

Interaction of radially polarized focused light with a prolate spheroidal nanoparticle

Kürşat Sendur and Ahmet Şahinöz

Sabancı University, Istanbul, 34956, Turkey

sendur@sabanciuniv.edu

Abstract: The interaction of a nanoparticle with light is affected by nanoparticle geometry and composition, as well as by focused beam parameters, such as the polarization and numerical aperture of the beam. The interaction of a radially focused beam with a prolate spheroidal nanoparticle is particularly important because it has the potential to produce strong near-field electromagnetic radiation. Strong and tightly localized longitudinal components of a radially polarized focused beam can excite strong plasmon modes on elongated nanoparticles such as prolate spheroids. In this study, near field radiation from a prolate spheroidal nanoparticle is investigated when it is illuminated with a radially polarized focused beam of light. Near-field radiation from the nanoparticle is investigated in the absence and presence of metallic layers. It is shown that the interaction of a radially polarized focused beam with a prolate spheroidal nanoparticle can be enhanced by creating images of monopole charges using metallic layers. In addition, it is also observed that the presence of a metallic layer shifts the resonance of the prolate spheroid toward longer wavelengths. Dipole, quadruple, and off resonance field distributions for particles with different sizes and aspect ratios are presented when they are illuminated with a radially focused beam of light.

© 2009 Optical Society of America

OCIS codes: (240.6680) Surface plasmons; (000.4430) Numerical approximation and analysis.

References and links

1. K. L. Kelly, E. Coronado, L. L. Zhao, and G. C. Schatz, "The optical properties of metal nanoparticles: The influence of size, shape, and dielectric environment," *J. Phys. Chem. B* **107**, 668–677 (2003).
2. O. Sqalli, I. Utke, P. Hoffmann, and F. Marquis-Weible, "Gold elliptical nanoantennas as probes for near field optical microscopy," *J. Appl. Phys.* **92**, 1078–1083 (2002).
3. W. A. Challener, I. K. Sendur, and C. Peng, "Scattered field formulation of finite difference time domain for a focused light beam in a dense media with lossy materials," *Opt. Express* **11**, 3160–3170 (2003).
4. K. Sendur, W. Challener, and O. Mryasov, "Interaction of spherical nanoparticles with a highly focused beam of light," *Opt. Express* **16**, 2874–2886 (2008).
5. J. Lermé, G. Bachelier, P. Billaud, C. Bonnet, M. Broyer, E. Cottancin, S. Marhaba, and M. Pellarin, "Optical response of a single spherical particle in a tightly focused light beam: application to the spatial modulation spectroscopy technique," *J. Opt. Soc. Am. A* **25**, 493–514 (2008).
6. N. M. Mojarad, V. Sandoghdar, and M. Agio, "Plasmon spectra of nanospheres under a tightly focused beam," *J. Opt. Soc. Am. B* **25**, 651–658 (2008).
7. D. Khoptyar, R. Gutbrod, A. Chizhik, J. Enderlein, F. Schleifenbaum, M. Steiner, A. J. Meixner, "Tight focusing of laser beams in a $\lambda/2$ -microcavity," *Opt. Express* **16**, 9907–9917 (2008).

8. A. V. Failla, H. Qian, H. H. Qian, A. Hartschuh, A. J. Meixner, "Orientational imaging of subwavelength Au particles with higher order laser modes," *Nano Lett.* **6**, 1374-1378 (2006).
9. N. M. Mojarad and M. Agio, "Tailoring the excitation of localized surface plasmon-polariton resonances by focusing radially-polarized beams," *Opt. Express* **17**, 117-122 (2009).
10. N. Calander and M. Willander, "Theory of surface-plasmon resonance optical-field enhancement at prolate spheroids," *J. Appl. Phys.* **92**, 4878-4884 (2002).
11. B. B. Goldberg, S. B. Ippolito, L. Novotny, Z. Liu, and M. S. Unlu, "Immersion lens microscopy of photonic nanostructures and quantum dots," *IEEE J. Sel. Top. Quantum Electron.* **8**, 1051-1059 (2002).
12. K. S. Youngworth and T. G. Brown, "Focusing of high numerical aperture cylindrical-vector beams," *Opt. Express* **7**, 77-87 (2000).
13. E. Wolf, "Electromagnetic diffraction in optical systems I. An integral representation of the image field," *Proc. Roy. Soc. London Ser. A* **253**, 349-357 (1959).
14. B. Richards and E. Wolf, "Electromagnetic diffraction in optical systems II. Structure of the image field in an aplanatic system," *Proc. Roy. Soc. London Ser. A* **253**, 358-379 (1959).
15. L. Novotny and B. Hecht, *Principles of nano-optics*, Chapter 3 (Cambridge University Press, New York, NY, 2006)
16. I. Ichimura, S. Hayashi, and G. S. Kino, "High-density optical recording using a solid immersion lens," *Appl. Opt.* **36**, 4339-4348 (1997).
17. R. Dorn, S. Quabis, and G. Leuchs, "Sharper focus for a radially polarized light beam," *Phys. Rev. Lett.* **91**, 233901 (2003).
18. M. J. Snadden, A. S. Bell, R. B. M. Clarke, E. Riis, and D. H. McIntyre, "Doughnut mode magneto-optical trap," *J. Opt. Soc. Am. B* **14**, 544-552 (1997).
19. S. C. Tidwell, D. H. Ford, and W. D. Kimura, "Generating radially polarized beams interferometrically," *Appl. Opt.* **29**, 2234-2239 (1990).
20. H. Kano, D. Nomura, and H. Shibuya, "Excitation of surface-plasmon polaritons by use of a zeroth-order Bessel beam," *Appl. Opt.* **43**, 2409-2411 (2004).
21. H. Kano, S. Mizuguchi, and S. Kawata, "Excitation of surface-plasmon polaritons by a focused laser beam," *J. Opt. Soc. Am. B* **15**, 1381-1386 (1998).
22. J. M. Jin, *The finite element method in electromagnetics* (John Wiley & Sons, New York, NY, 2000).
23. All the FEM calculations in this report are performed with High Frequency Structure Simulator from Ansoft Inc with the inhouse developed focused beam models integrated into it.
24. E. D. Palik, *Handbook of optical constants of solids* (Academic Press, San Diego, CA, 1998).
25. A. Hartschuh, E. J. Sánchez, X. S. Xie, and L. Novotny, "High-resolution near-field Raman microscopy of single-walled carbon nanotubes," *Phys. Rev. Lett.* **90**, 095503 (2003).
26. K. Sendur, W. Challener, and C. Peng, "Ridge waveguide as a near field aperture for high density data storage," *J. Appl. Phys.* **96**, 2743-2752 (2004).
27. L. Wang and X. Xu, "Numerical study of optical nanolithography using nanoscale bow-tie-shaped nano-apertures," *J. Microsc.* **229**, 483-489 (2008).
28. B. Liedberg, C. Nylander, and I. Lundstroem, "Surface plasmon resonances for gas detection and biosensing," *Sens. Actuators* **4**, 299-304 (1983).
29. J. A. Kong, *Electromagnetic wave theory* (Wiley, New York, NY, 1990).
30. P. Nordlander and E. Prodan, "Plasmon hybridization in nanoparticles near metallic surfaces," *Nano Lett.* **4**, 2209 (2004).
31. F. Le, N. Z. Lwin, J. M. Steele, M. Kil, N. J. Halas, and P. Nordlander, "Plasmons in the metallic nanoparticle-film system as a tunable impurity problem," *Nano Lett.* **5**, 2009 (2005).

1. Introduction

The interaction of photons with metallic nanoparticles is important to a number of emerging nanotechnology applications due to the large enhancement and tight localization of electromagnetic fields in the vicinity of nanoparticles. In addition, the spectral response of the geometry coupled plasmon resonances of a nanoparticle is tightly distributed, therefore, making it relevant for applications that require high sensitivity. These resonances can be engineered to the desired specifications by utilizing the shape and size of the nanoparticles, as well as the dielectric properties of the surrounding medium [1, 2].

Although experimental studies in the literature have used both collimated and focused beams to excite surface plasmons, until recently the analytical and numerical models in the literature have only used simple plane waves to analyze this interaction. Recently, there has been increasing interest in understanding the interaction of a focused beam of light with a nanoparticle.

Numerical techniques based on finite difference time-domain [3] and finite element method [4], as well as analytical techniques based on generalized Mie theory have been used [4, 5, 6] to analyze the interaction of a focused beam with a nanoparticle. Challener et al. [3] developed a finite difference time domain code to analyze the interaction of a linearly polarized focused beam with a spherical nanoparticle located in a high refractive index medium. More recently, detailed analytical models have been published by Lerme et al. [5], Sendur et al. [4], and Mojarad et al. [6] based on generalized Mie theory. In these studies, a linearly polarized focused beam has been used to study the interaction of focused light with nanoparticles [3, 4, 5, 6]. There have been theoretical and extensive experimental studies on the interaction of radially polarized focused light with nanostructures such as spheres and rods [7, 8]. Sendur et al. [4] extended the generalized Mie theory formulation to the case where a radially polarized focused beam illuminates a spherical nanoparticle. In a more recent study Mojarad et al. [9] used a radially polarized focused beam to tailor the localized surface plasmon spectra of nanoparticles.

The aforementioned studies [3, 4, 5, 6] employ only spherical particles to study the interaction of a focused beam and nanoparticles. Elongating the nanoparticle can provide further electric field enhancement for particles excited at the plasmon resonance condition, as shown for the spheroids illuminated with a plane wave excitation [10]. The interaction of a radially focused beam with elongated particles, such as a prolate spheroidal nanoparticle, is particularly interesting because it has the potential to produce even stronger near-field electromagnetic radiation. As illustrated by Goldberg et al. [11], a tip-like aluminum particle with an elongated axis in the propagation direction of a radially polarized beam can provide strong and localized electromagnetic radiation. However, the impact of the metallic layer on the interaction of a prolate spheroidal nanoparticle with radially polarized light has not been studied. The presence of such a layer can further enhance the near-field radiation from the nanoparticle. In addition, the presence of such a layer causes a spectral shift in the resonance wavelength, as shown in this study.

In this study, the interaction between a radially polarized focused beam of light and a prolate spheroidal nanoparticle is investigated. This study provides an extension of the current knowledge of the interaction of focused light with nanoparticles by adding the effect of nanoparticle shape and radial incident beam polarization. This study investigates how beams with various angular spectra interact with prolate spheroidal nanoparticles. A new configuration is suggested to further improve the near-field radiation from a prolate spheroid nanoparticle by creating an image of the localized charge at the tip of the particle. A detailed parameter investigation is carried out to study the optimal shapes and sizes of prolate spheroidal nanoparticles, as well as optimum focused beam parameters. This study is organized as follows: In Sect. 2, prolate spheroidal particles used in this study are discussed. The incident radially polarized focused beam is also discussed in Sect. 2 along with illustrations of various field components. In Sect. 3, various factors that impact the interaction of a prolate spheroid nanoparticle with a radially polarized focused beam of light are discussed. In particular, the parameters related to particle geometry, material composition, and excitation source are investigated in detail. In Sect. 4, a prolate spheroidal nanoparticle configuration is discussed to further improve the near-zone electric fields in the vicinity of the particle. Concluding remarks appear in Sect. 5.

2. Prolate spheroid and radially polarized focused beam

Particles with large aspect ratios can support strong plasmon modes when they are illuminated with longitudinal fields. A radially polarized focused beam has a very strong longitudinal component in the direction of propagation [12]. The strong longitudinal component of radial polarization can excite strong plasmon resonances on a prolate spheroidal nanoparticle with a major axis aligned in the direction of the propagation of the focused beam. A prolate spheroid

can be defined as

$$\begin{bmatrix} x \\ y \\ z \end{bmatrix} = \begin{bmatrix} a \sinh \xi \sin \theta \cos \phi \\ a \sinh \xi \sin \theta \sin \phi \\ a \cosh \xi \cos \theta \end{bmatrix}; \quad 0 \leq \theta \leq \pi, \quad 0 < \phi \leq 2\pi \quad (1)$$

where a determines the size of the particle, and $\tanh \xi$ determines the minor to major axis ratio of the particle. The minor axis b of the prolate particle is obtained by $b = a \tanh \xi$. The ξ values that are used in this study are 0.2, 0.3, 0.4, 0.5, and 0.6. These ratios correspond to minor to major axis ratios of 0.197, 0.291, 0.38, 0.462, and 0.537, respectively.

Since the excitation of the plasmons of nanoparticles relies on the light of specific polarizations, considering an accurate description of the incident beam that accounts for the vector nature of the focused beam is extremely important. To obtain an accurate representation of a radially polarized tightly focused beam of light, the theory established by Richards and Wolf [13, 14] is used. In this approach, rays that are incident onto a lens are collected and focused based on the rules of Geometric Optics. After each ray is diffracted by the lens system, the overall contribution is calculated by summing up the individual rays. Formulas based on the Richards and Wolf vector field theory have been previously used in the literature [3, 4, 12, 15, 16] for focused beams of various polarizations. In addition, practical aspects of radially polarized focused light have been discussed in the literature [17, 18, 19, 20, 21].

Using Richards and Wolf [13, 14] theory, the total electric field for a radially polarized beam of light near the focus is given as [12]

$$\mathbf{E}(\mathbf{r}_p) = -\frac{i}{\lambda} \int_0^\alpha d\theta \sin \theta \sqrt{\cos \theta} \int_0^{2\pi} d\phi \begin{bmatrix} \cos \theta \cos \phi \\ \cos \theta \sin \phi \\ \sin \theta \end{bmatrix} \exp(-i\mathbf{k} \cdot \mathbf{r}_p) \quad (2)$$

where an apodization function of $\sqrt{\cos \theta}$ is used in this study and no additional apodization filters are applied at the pupil plane. In Eq. (2) \mathbf{r}_p is the observation point

$$\mathbf{r}_p = x_p \hat{x} + y_p \hat{y} + z_p \hat{z} = r_p \cos \phi_p \hat{x} + r_p \sin \phi_p \hat{y} + z_p \hat{z} \quad (3)$$

and \mathbf{k} is the wavevector

$$\mathbf{k} = \frac{2\pi}{\lambda} (\sin \theta \cos \phi \hat{x} + \sin \theta \sin \phi \hat{y} - \cos \theta \hat{z}), \quad (4)$$

where λ is the wavelength in the medium, $r_p = \sqrt{x_p^2 + y_p^2}$, and $\phi_p = \arctan(y_p/x_p)$. In this representation, each ray is identified by a θ and ϕ depending on its incidence angle.

Only the rays incident on the lens can be collected. Any lens has a finite size, therefore, the rays beyond the size of the lens cannot be focused by the lens system. The half-beam angle α represents the cone angle within which the rays can be collected. The half-beam angle imposes a cut-off to the upper limit of the integral in Eq. (2). The physical configuration of the lens system and the size of the lenses determine this cut-off angle. The cut-off angle determines which rays contribute to the radially polarized focused beam. Therefore, the half-beam angle incorporates the physics of the lens system into Eq. (2). The finite size of the lens results in the integral in Eq. (2) having an upper limit $\theta = \alpha$ where $\alpha < \pi/2$. To make use of the full numerical aperture of the lens system, the incident beam is assumed to fill the back-aperture of the lens system.

In Fig. 1, different field components of radially polarized focused beams with various α are illustrated. The beams are focused onto the \hat{x} - \hat{y} plane and propagate in the \hat{z} direction with the focal point at (0, 0, 0). The wavelength is 700 nm. The transverse components, E_x and E_y , and

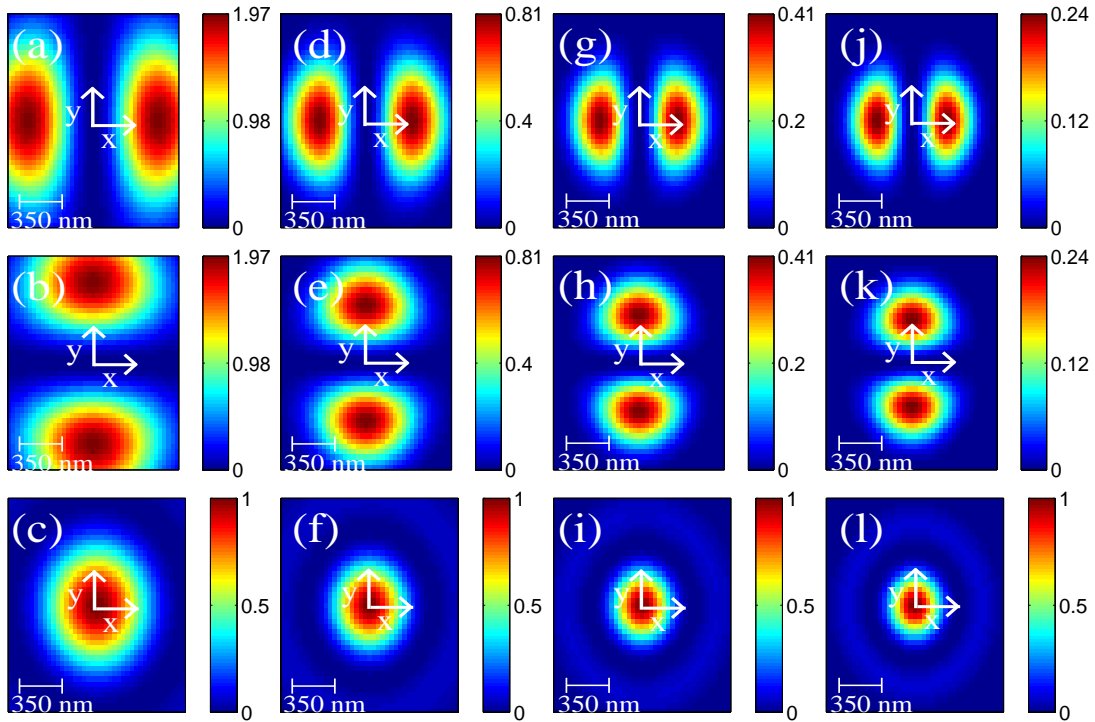


Fig. 1. The field components for a radially polarized focused beam with various α : (a) E_x for $\alpha = 30^\circ$, (b) E_y for $\alpha = 30^\circ$, (c) E_z for $\alpha = 30^\circ$, (d) E_x for $\alpha = 45^\circ$, (e) E_y for $\alpha = 45^\circ$, (f) E_z for $\alpha = 45^\circ$, (g) E_x for $\alpha = 60^\circ$, (h) E_y for $\alpha = 60^\circ$, (i) E_z for $\alpha = 60^\circ$, (j) E_x for $\alpha = 75^\circ$, (k) E_y for $\alpha = 75^\circ$, (l) E_z for $\alpha = 75^\circ$.

the longitudinal component E_z are plotted for α values of 30° , 45° , 60° , and 75° . The results are normalized with respect to the maximum value of the longitudinal component on the \hat{x} - \hat{y} plane. As the half-beam angle increases, the amplitude of the longitudinal component becomes larger compared to the amplitude of the transverse components. In addition, the longitudinal component becomes more tightly focused around the focal point as α increases. Figure 1 illustrates the typical radially polarized incident beam distributions that will be used to illuminate prolate spheroid particles in this study.

3. Near-field radiation from a prolate spheroid

In this section, we investigate the interaction of a prolate spheroid nanoparticle with a radially polarized focused beam of light in the absence of any metallic layers in the vicinity of the nanoparticle. To analyze this interaction, a 3-D finite element method (FEM) based full-wave solution of Maxwell's equations is used [22, 23]. Radiation boundary conditions are used in FEM simulations. To represent the scattering geometries accurately, tetrahedral elements are used to discretize the computational domain. On the tetrahedral elements, edge basis functions and second-order interpolation functions are used to expand the functions. Adaptive mesh refinement is used to improve the coarse solution regions with high field intensities and large field gradients. The validity of the method was previously tested with an analytical solution based on generalized Mie theory [4].

In Fig. 2(a) a schematic illustration of a prolate spheroidal nanoparticle and the incident ra-

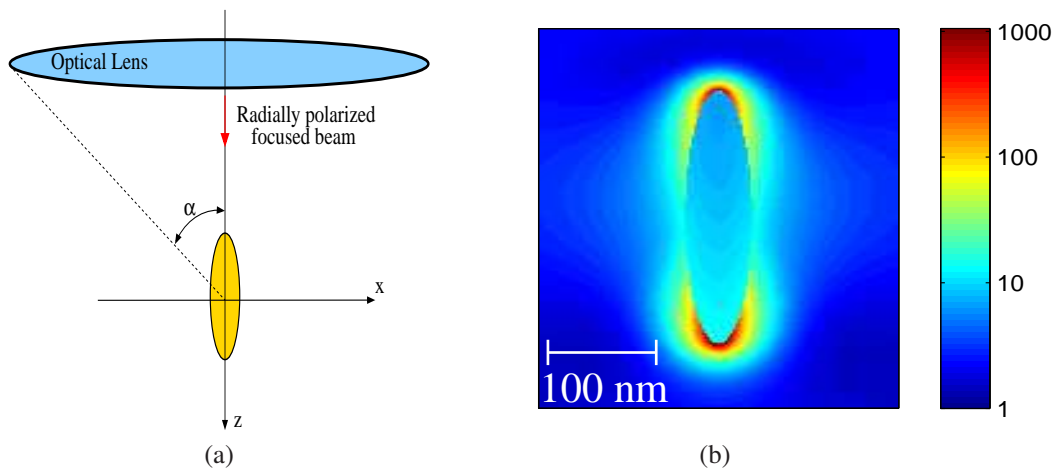


Fig. 2. (a) A schematic illustration of a prolate spheroidal nanoparticle and the incident radially polarized focused beam. The red arrow illustrates the propagation direction of the beam. (b) $|\mathbf{E}(\mathbf{r})|^2$ distribution on the \hat{x} - \hat{z} cut plane for a gold prolate spheroid particle of $a = 100$ nm and $\xi = 0.2$ illuminated with a radially polarized focused light at $\lambda = 700$ nm.

dially polarized focused beam is provided. In this schematic illustration a red arrow illustrates the propagation direction of the beam. The same convention for the propagation direction and nanoparticle orientation is used in the remainder of the simulations. In Fig. 2(b), the total intensity profile is plotted on the \hat{x} - \hat{z} plane, which passes through the center of the prolate spheroid particle. The incident beam is focused onto the \hat{x} - \hat{y} plane and propagates in the \hat{z} direction. The focal point of the incident beam corresponds to the center of the nanoparticle. The wavelength of incident light is 700 nm. The half beam angle of the focused beam is $\alpha = 60^\circ$, which corresponds to a numerical aperture of 0.86. Various components of the incident focused beam were previously illustrated in Fig. 1(g)-(i). The prolate spheroid particle is made of gold, with the optical properties of gold and silver used in this study retrieved from the literature [24]. The geometric parameters defining the prolate spheroid in Fig. 2(b) are $a = 100$ nm and $\xi = 0.2$.

$|\mathbf{E}(\mathbf{r})|^2$ distribution on the \hat{x} - \hat{z} cut plane is plotted in Fig. 2(b) for the parameters summarized in the previous paragraph. All the field intensities reported in this paper are normalized with respect to the intensity of the focused beam at the focal point. Therefore, the quantities reported in the manuscript correspond to intensity enhancement. As shown in Fig. 2(b), a very tightly localized near-field electromagnetic radiation is obtained at the tip of the prolate spheroidal gold nanoparticle. A very large electromagnetic field enhancement is also observed at the tips of the nanoparticle. The main reason for the large field enhancement at the tips of the nanoparticle is the strong and tightly localized longitudinal component obtained from a radially polarized focused beam. This longitudinal component for high numerical aperture beams, which was previously illustrated in Fig. 1, is very desirable to excite plasmon resonances on a prolate spheroidal nanoparticle. The longitudinal orientation of the focused beam is favorable for the shape and orientation of prolate spheroid nanoparticles with the main axis oriented in the longitudinal direction. In addition, the slowly tapered tip provides further enhancement of the electric field in the vicinity of the tip, as shown in Fig. 2(b). The localized optical energy at the tip of the prolate spheroid, and the interaction between the prolate spheroid nanoparticle and nearby objects have potential applications at the nanoscale, including near-field scanning optical microscopy [25], high-density data storage [26], nano-lithography [27], and bio-chemical sensing [28]. For this simulation, in which the particle size is much smaller than the wavelength of light, the field

enhancement is observed on both tips of the nanoparticle. However, the enhancement at the tip in the propagation direction is slightly higher. As seen in later simulations, the asymmetry becomes more prominent for larger particles.

Particle-plasmons on a metallic prolate spheroid are a result of the plasma oscillations in the entire particle volume. Effective coupling of plasmons into a metallic spheroidal nanoparticle depends primarily on two factors: a large aspect ratio of the spheroid and a strong polarization component of the incident field along the major axis of the nanoparticle. The polarization component of the incident field along the major axis of the prolate spheroid causes a collective oscillation of the electrons, which gives rise to the plasmon resonance of the particle. Once these conditions are satisfied, the exact size and shape of the particle can be tuned to support plasmon resonances on nanoparticles. The tuning of the particle geometry is determined by a and ξ , whereas the tuning of the incident beam is determined by the wavelength and numerical aperture of the incident beam.

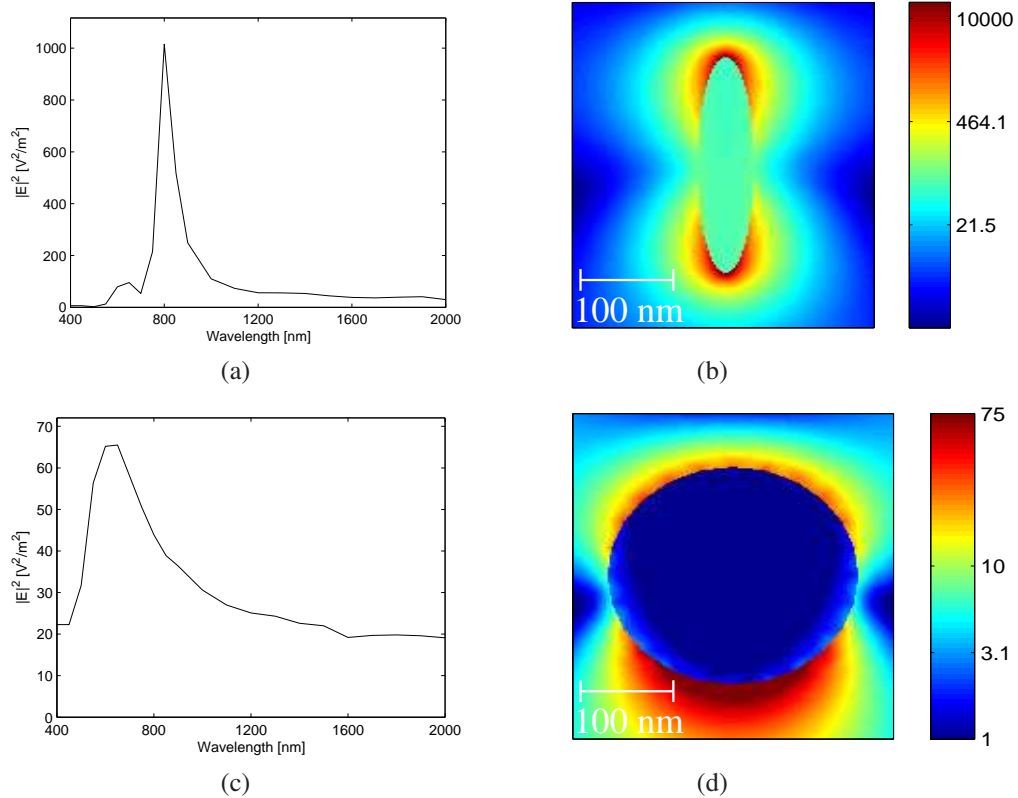


Fig. 3. (a) The wavelength response of a gold prolate spheroidal nanoparticle with $a = 100$ nm and $\xi = 0.2$ is plotted. The intensity $|\mathbf{E}|^2$ is calculated at a distance 10 nm away at various wavelengths. (b) $|\mathbf{E}(\mathbf{r})|^2$ distribution on the \hat{x} - \hat{z} cut plane is plotted at $\lambda = 800$ nm for a gold prolate spheroid with $a = 100$ nm and $\xi = 0.2$. (c) The wavelength response of a gold spherical nanoparticle with a radius of 100 nm is plotted. The intensity $|\mathbf{E}|^2$ is calculated at a distance 10 nm away at various wavelengths. (d) $|\mathbf{E}(\mathbf{r})|^2$ distribution on the \hat{x} - \hat{z} cut plane is plotted at $\lambda = 650$ nm for a gold spherical nanoparticle with a radius of 100 nm.

The near-field radiation from a gold prolate spheroid and a sphere are compared in Fig. 3. First, the wavelength response of a gold prolate spheroid nanoparticle with $a = 100$ nm and $\xi = 0.2$ is plotted in Fig. 3(a). The results suggest that the maximum near-field radiation is obtained at $\lambda = 800$ nm. In Fig. 3(b), $|\mathbf{E}(\mathbf{r})|^2$ distribution on the x-z cut plane is plotted at $\lambda = 800$ nm. A similar calculation is repeated for the gold spherical nanoparticle in Figs. 3(c) and (d). The maximum near-field radiation for the spherical particle is obtained at $\lambda = 650$ nm. A comparison of the peak fields in Fig. 3 suggest that the prolate spheroid provides significantly larger localized near field radiation compared to a sphere.

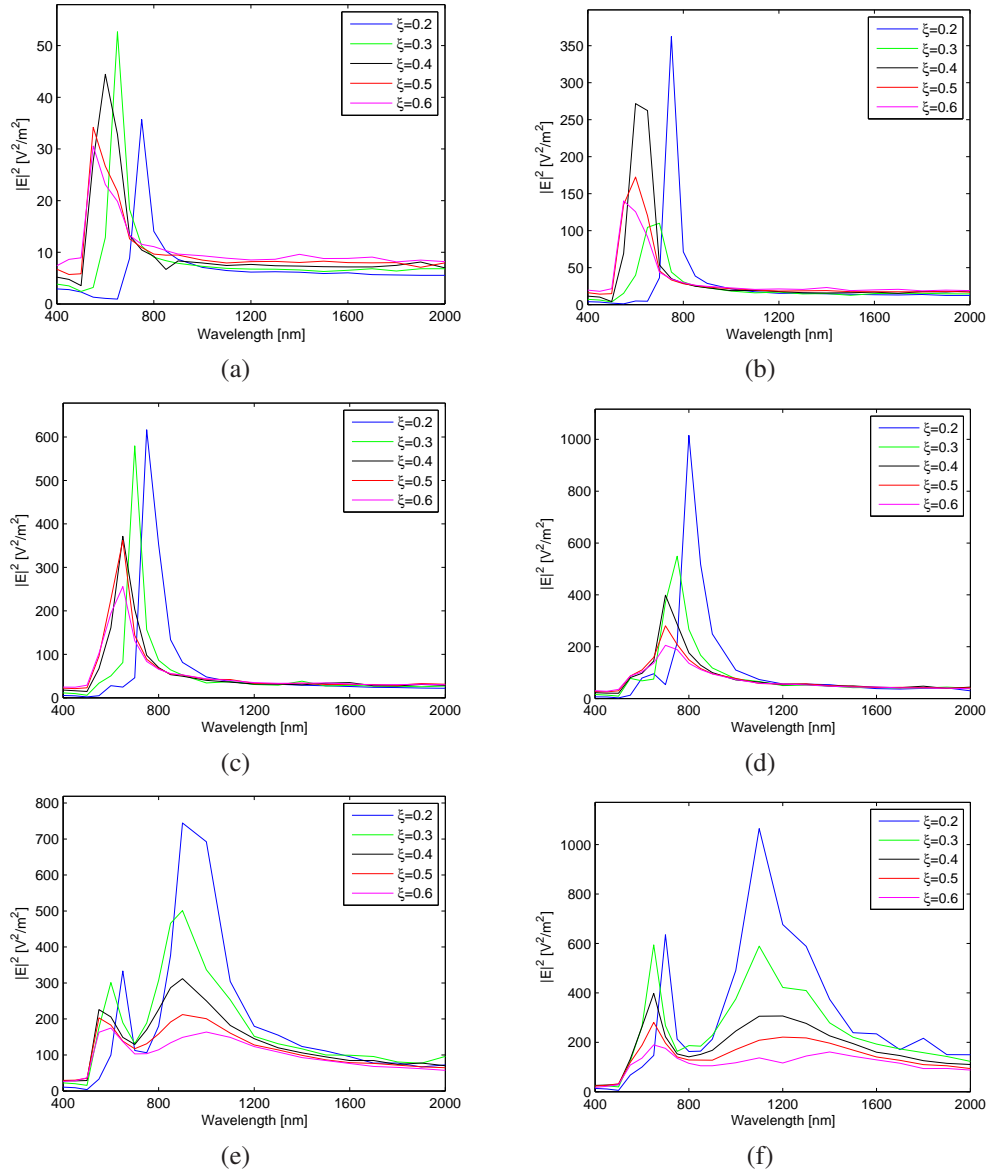


Fig. 4. The intensity $|\mathbf{E}|^2$ at a distance 10 nm away from the tip of a gold nanoparticle for various prolate sizes: (a) $a = 25$ nm, (b) $a = 50$ nm, (c) $a = 75$ nm, (d) $a = 100$ nm, (e) $a = 150$ nm, (f) $a = 200$ nm.

As mentioned, the wavelength of light, geometry and composition of nanoparticles can be adjusted to support strong plasmon resonances on these structures. Next we investigate the impact of these factors on the interaction of radially polarized focused light with prolate spheroid particles. The parameters that are investigated can be divided into 3 main categories:

1. Geometric factors, a and ξ ;
2. Source dependent parameters, wavelength λ and half-beam angle α ;
3. Material composition of the nanoparticle.

A study of the geometric parameters and source dependent factors is summarized in the rest of this section. The material compositions of the particles in this study are limited to gold and silver.

First, we studied the impact of geometric factors a , ξ , and the wavelength of the optical source λ . The nanoparticle composition is selected as gold. The numerical aperture of the lens system is selected as 0.86. In Fig. 4, the intensity $|\mathbf{E}|^2$ at a distance of 10 nm away from the tip of a gold nanoparticle is plotted for various prolate spheroids. In Figs. 4(a)-(f) the intensity is given for particle sizes of $a=25, 50, 75, 100, 150,$ and 200 nm, respectively. At each particle size, the intensity is plotted as a function of wavelength for ξ values of 0.2, 0.3, 0.4, 0.5, and 0.6. The results show that the electric field intensity increases for reducing ξ , which can be explained by two factors. The first factor is the lightning rod effect. As ξ gets smaller, the aspect ratio of the particle increases and the tip of the particle becomes sharper, resulting in larger intensity values in the vicinity of the nanoparticle. The second factor is that as ξ gets smaller, the aspect ratio of the particle becomes larger, which is more favorable for exciting plasmon resonances on elongated nanoparticles via the strong longitudinal component of the radially polarized focused beam. The results in Fig. 4(a)-(d) indicate that the dipolar resonances are dominant for particle sizes of $a=25, 50, 75,$ and 100 nm. As the particle size is increased beyond 150 nm, the quadruple resonances become stronger, as shown in Fig. 4(e)-(f). The

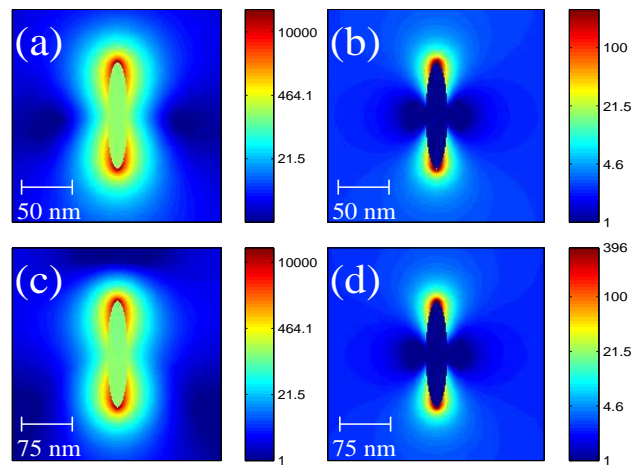


Fig. 5. $|\mathbf{E}(\mathbf{r})|^2$ distributions for prolate spheroids with $\xi = 0.2$. The distributions are given for various prolate sizes and at various wavelengths [a (nm), λ (nm)]: (a) [50, 750], (b) [50, 1600], (c) [75, 750], and (d) [75, 1600]. Note that the left column corresponds to dipolar resonance points, whereas the right column corresponds to off resonance points.

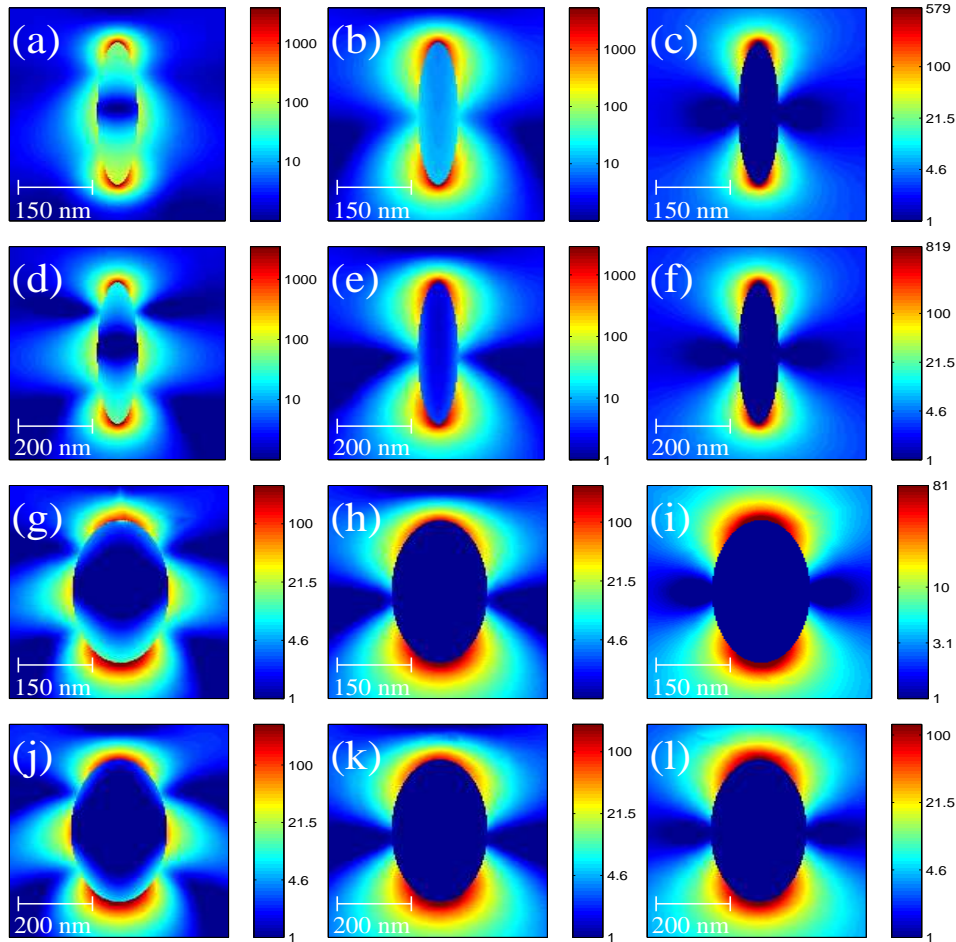


Fig. 6. $|\mathbf{E}(\mathbf{r})|^2$ distributions for various prolate spheroids with $\xi = 0.2$. The distributions are given for various prolate sizes and at various wavelengths [a (nm), ξ , λ (nm)]: (a) [150, 0.2, 650], (b) [150, 0.2, 900], (c) [150, 0.2, 1600], (d) [200, 0.2, 700], (e) [200, 0.2, 1100], (f) [200, 0.2, 1600], (g) [150, 0.5, 550], (h) [150, 0.5, 900], (i) [150, 0.5, 1600], (j) [200, 0.5, 650], (k) [200, 0.5, 1200], and (l) [200, 0.5, 1600]. Note that the left column corresponds to quadruple resonance points, the middle column corresponds to dipolar resonance points, and the right column corresponds to off resonance points.

results in Fig. 4 indicate that the plasmonic resonances of nano-particles demonstrate a red-shift as the ξ values are decreased. This observation is in agreement with the red-shift reported in high-aspect nanoparticles [1].

In Figs. 5 and 6 the electric field intensity distributions are plotted for various prolate spheroid nanoparticles when they are excited at the wavelengths corresponding to dipolar-resonance, off-resonance, and quadruple resonance. Small prolate spheroids with $a = 25$ nm, $a = 50$ nm, and $a = 75$ nm do not demonstrate any quadruple resonance points, as shown in Fig. 4. Therefore, the results in Fig. 5 illustrate the near-field distributions for prolate spheroids excited at the dipolar resonance and off-resonance frequency points. In Fig. 5 the left column illustrates dipolar resonance intensity distributions, whereas the right column shows the off resonance intensity

distributions. The top and bottom rows correspond to particles with $a = 50$ nm and $a = 75$ nm, respectively.

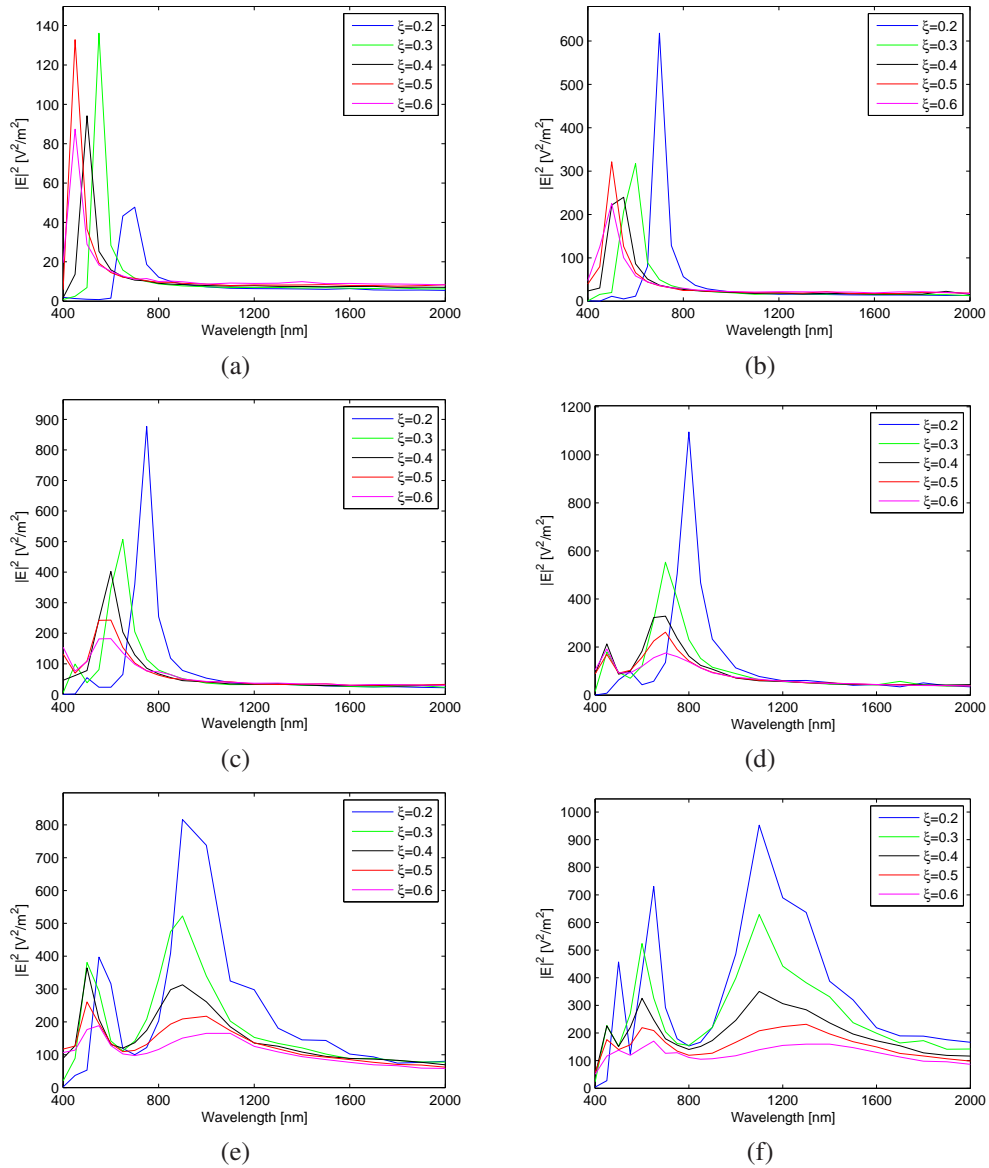


Fig. 7. The intensity $|E|^2$ at a distance 10 nm away from the tip of a silver nanoparticle for various prolate sizes: (a) $a = 25$ nm, (b) $a = 50$ nm, (c) $a = 75$ nm, (d) $a = 100$ nm, (e) $a = 150$ nm, (f) $a = 200$ nm.

As mentioned previously, quadruple resonance points were identified only for large spheroids. Figures 6(a)-(l) illustrate the dipolar resonance, quadruple resonance, and off-resonance distributions for particles with $a=150$ nm and $a=200$ nm. Figures 6(a), (d), (g), and (j) illustrate the quadruple resonance for particles with $[a$ (nm), ξ]= [150,0.2], [200,0.2], [150,0.5], and [200,0.5]. Dipolar-resonance distributions are provided in Figs. 6(b), (e), (h), and (k), respectively. Note that the left column corresponds to quadruple resonance points, the middle

column corresponds to dipolar resonance points, and the right column corresponds to off resonance points. A comparison of the dipolar and quadruple distributions suggest that the field distributions at quadruple resonance also have strong lobes on the x-axis. These lobes are stronger for larger ξ and a values. The peak at 600-700 nm shows all of the features of quadruple resonance. It is very small for small particles, and becomes more dominant for larger particles as the particle size increases. Four peaks are identified over the structure, and there is 90° separation between the peaks. The major difference of the quadruple distribution of a spheroidal particle from that of a spherical particle is that the peaks shift 45° . The shift is due to the forced peaks at the tips of the nanoparticle. The tip of the nanoparticle forces the peaks to appear at the tips, which creates a shift in the quadruple distribution compared to a spherical particle.

The impact of changing the material composition of the prolate spheroidal nanoparticle to silver is studied in Fig. 7. The intensity $|\mathbf{E}|^2$ at a distance 10 nm away from the tip of a silver nanoparticle is plotted for various prolate spheroids. A comparison of the results in Fig. 4 and Fig. 7 suggest that changing the material composition of the nanoparticle has little impact on the resonance conditions. The electric field intensity is slightly higher for the silver nanoparticles, however, the resonance wavelength showed very little change.

A comparison of the spectral response of the radially polarized focused beam, a plane wave (polarized in the main axis of the prolate spheroid), and a linearly polarized focused beam (polarized in the main axis of the prolate spheroid) is illustrated in Fig. 8. The simulations are performed for two different prolate spheroids: $(a, \xi)=(200, 0.3)$ and $(a, \xi)=(200, 0.4)$. The results indicate that there are substantial differences between radially polarized focused beam and the other two illuminations. These differences are more prominent especially for larger spheroids.

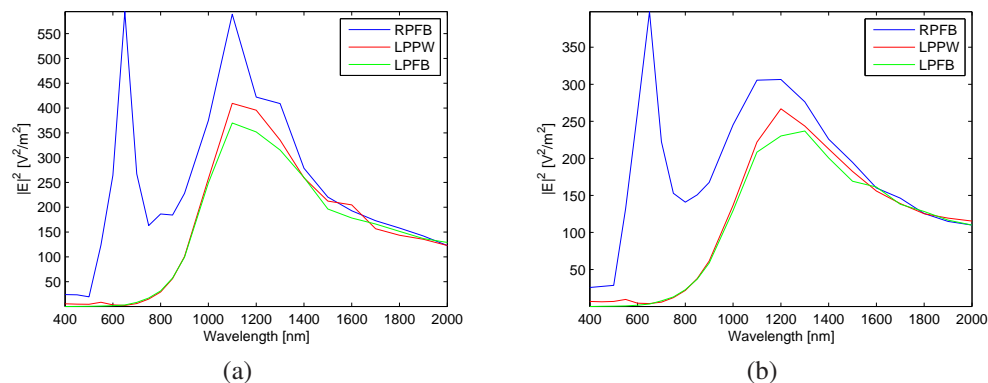


Fig. 8. A comparison of the spectral distribution from a gold prolate spheroidal nanoparticle illuminated with a radially polarized focused beam (RPFb), linearly polarized plane wave (LPPW), and linearly polarized focused beam (LPFB) for two different (a, ξ) pairs (a) (200, 0.3) and (b) (200, 0.4).

In the final set of results in this section, the impact of the angular spectrum distribution of the incident radially polarized beam on the plasmons of spheroidal nanoparticles is studied. Two different parameters sets are selected: $[a \text{ (nm)}, \xi, \lambda \text{ (nm)}] = [150, 0.2, 650]$ and $[150, 0.2, 900]$. The former set of parameters corresponds to the quadruple resonance point, while the latter corresponds to the dipolar resonance point. In Fig. 9 and Fig. 10 the electric field distributions on the prolate spheroid nanoparticle are plotted for parameters $[a \text{ (nm)}, \xi, \lambda \text{ (nm)}] = [150, 0.2, 650]$ and $[150, 0.2, 900]$, respectively. In both figures the incident beam is a radially focused beam with half-beam angles $\alpha = 15^\circ, 30^\circ, 45^\circ,$ and 60° . For both cases, while the electric

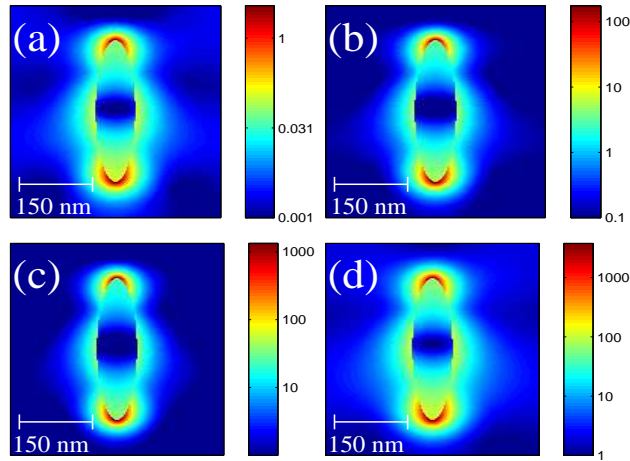


Fig. 9. $|\mathbf{E}(\mathbf{r})|^2$ distributions for a gold prolate spheroid with $[a \text{ (nm)}, \xi, \lambda \text{ (nm)}] = [150, 0.2, 650]$. The distributions are given for various half-beam angle: (a) $\alpha = 15^\circ$, (b) $\alpha = 30^\circ$, (c) $\alpha = 45^\circ$, and (d) $\alpha = 60^\circ$.

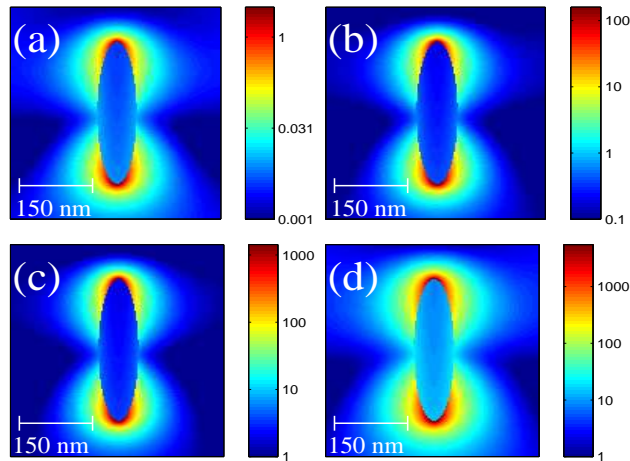


Fig. 10. $|\mathbf{E}(\mathbf{r})|^2$ distributions for a gold prolate spheroid with $[a \text{ (nm)}, \xi, \lambda \text{ (nm)}] = [150, 0.2, 900]$. The distributions are given for various half-beam angle: (a) $\alpha = 15^\circ$, (b) $\alpha = 30^\circ$, (c) $\alpha = 45^\circ$, and (d) $\alpha = 60^\circ$.

field distribution does not change as the half-beam angle is increased, the amplitude of the near-field electric field distribution increases as the half-beam angle is increased. The angular spectrum of the incident beam is tight for $\alpha = 15^\circ$, becoming wider as the half beam angle is increased. Therefore, the incident wave amplitude onto the particle increases as the half-beam angle increases. As a result of increasing the incident field amplitude, the scattered field amplitude also increases, as shown in Figs. 9 and 10.

4. Impact of a metallic layer

It is possible to further improve the near field radiation from the prolate spheroidal nanoparticle by placing a metallic layer as shown in Fig. 11(a). As described in the previous section, the induced current over a metallic structure results in a charge accumulation at the end of the spheroid nanoparticle. The oscillation of this monopole gives rise to localized near-field radiation. By placing a metallic layer, such as a gold layer, as shown in Fig. 11(a), it is possible to create an image of the monopole as shown in Fig. 11(b). The schematic illustration in Fig. 11(b) is equivalent to Fig. 11(a). Due to image theory [29], the metallic layer gives rise to another monopole. The original monopole and its image in the metallic layer create an electric dipole. The resulting electric dipole radiates stronger than the electric monopole at the tip of the prolate spheroid in the absence of a metallic layer.

A comparison of the near-field radiation of a prolate spheroid nanoparticle in the absence and presence of a metallic layer is presented in Fig. 12. The total intensity profile is plotted in Fig. 12(a) on the \hat{x} - \hat{z} plane for a particle in the absence of a metallic layer. All simulation parameters are identical to the simulations in Figs. 12(b) and (c) with the exception of the presence of the 100 nm thick gold layer. The distance between the tip and the metallic layer are 5 nm and 10 nm in Figs. 12(b) and (c), respectively. The field enhancement due to the metallic layer can be seen by comparing the simulation results in Fig. 12. An important parameter that impacts the field strength in Fig. 12 is the distance between the prolate spheroidal particle and the gold layer. This distance determines the distance between the electric charges in the dipole

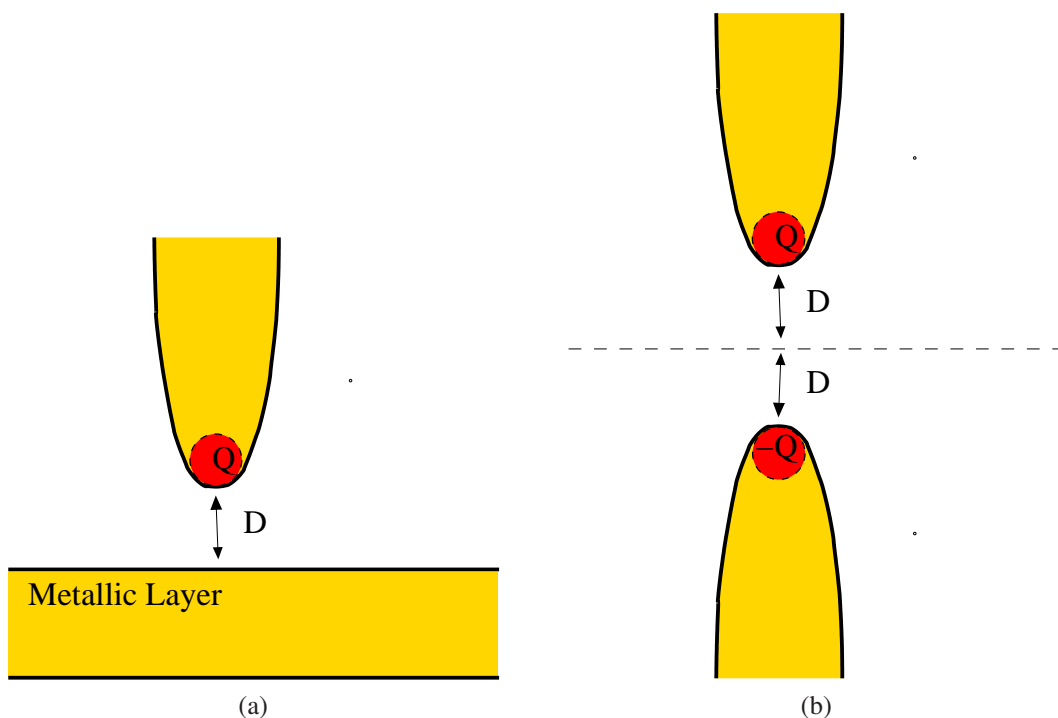


Fig. 11. (a) A schematic illustration of a prolate spheroidal nanoparticle in the presence of a metallic layer. The red circle and letter Q at the tip of prolate spheroid represents the charge accumulation created by the induced current due to the incident electromagnetic radiation. (b) An equivalent representation is illustrated. The metallic layer is replaced with another prolate spheroidal particle at a distance D from the interface using image theory.

configuration, therefore, impacting the near-field radiation strength of the electric dipole. In Fig. 13(a) the effect of the distance between the prolate spheroid and metallic layer on the near-field radiation is plotted. In the presence of the metallic layer, the distance is taken as 5 nm above the metal layer. The data is extracted from the graphs in Fig. 12. Weaker near-field radiation is observed for a large separation between the prolate spheroid and the metallic layer.

The presence of the metallic layer impacts the frequency response of the prolate spheroidal nanoparticle. In Fig. 13(b) the normalized intensity is plotted as a function of wavelength in the absence and presence of the metallic layer. All other parameters in the simulations are identical. Figure 13(b) suggest that the presence of a metallic layer shifts the resonances toward longer wavelengths, which is a similar trend observed in the literature [30, 31]. This can be best interpreted with the aid of Fig. 11. In the presence of a metallic layer, the particle and its image, as shown in Fig. 11(b), interact with the incident light. Therefore, the resulting resonant structure in the presence of the metallic layer is longer than the resonant structure in the absence of the metallic structure. The interaction of a higher aspect ratio particle with light results in a resonance shift toward longer wavelengths.

5. Conclusion

The interaction of a radially polarized focused beam of light and a prolate spheroidal nanoparticle is studied. In this study, the effect of particle geometry and composition, as well as focused beam parameters such as the numerical aperture of a beam and the wavelength of incident light are studied. When the particle is elongated in the direction of the strong component of the incident focused light, the amplitude over the particle increases as the half-beam angle is increased. The location and the relative amplitude of the lobes with respect to each other did not change by varying the angular spectrum of the incident beam. It was found that the presence of a metallic layer increases the near field radiation from the nanoparticle by creating an image of the oscillation charge monopole, and therefore, forming a strong dipole. The distance between the prolate spheroidal particle and the metallic layer impacts the field strength of the near-field radiation. It is also observed that the presence of a metallic layer shifts the resonance of the prolate spheroid toward longer wavelengths. The presence of the metallic layer results in a longer aspect ratio of the resonant structure, and therefore, moves the resonance wavelength. Dipolar, quadruple, and off resonance field distributions for particles with different size and aspect ratio are presented when they are illuminated with a radially focused beam of light. Small particles with sizes smaller than 75 nm demonstrated only dipole resonances. A comparison of the dipolar and quadruple distributions for larger particles suggest that the field distributions at quadruple resonance have strong lobes on the perpendicular axis.

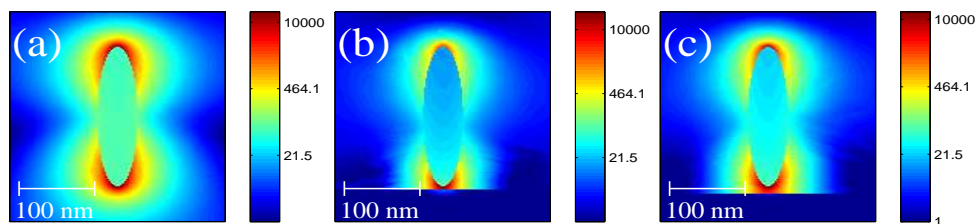


Fig. 12. $|\mathbf{E}(\mathbf{r})|^2$ distribution on the \hat{x} - \hat{z} cut plane for a gold prolate spheroid particle of $a = 100$ nm and $\xi = 0.2$ illuminated with a radially polarized focused light at $\lambda = 800$ nm. The particle is (a) in the absence of any metallic layers, (b) in the presence of a 100 nm gold layer placed 5 nm, and (c) 10 nm away from the tip of the nanoparticle.

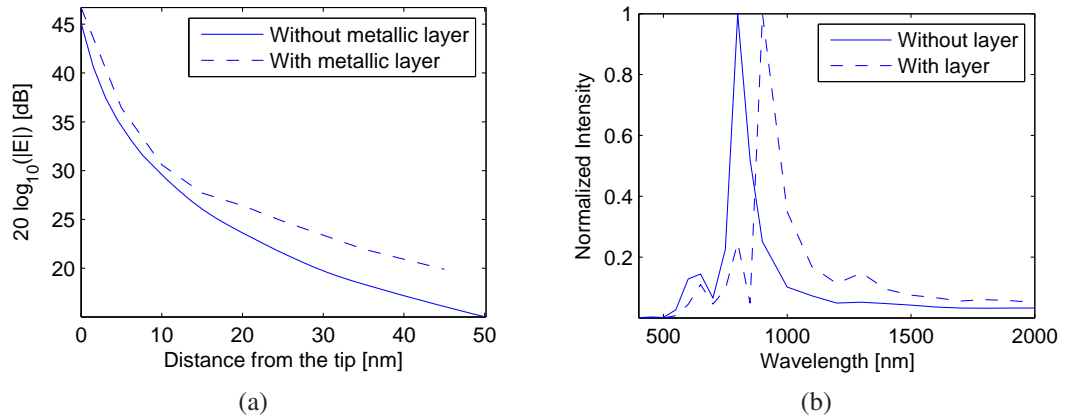


Fig. 13. (a) $|\mathbf{E}(\mathbf{r})|^2$ distribution as a function of distance from the tip of a gold prolate spheroid particle of $a = 100$ nm and $\xi = 0.2$ illuminated with a radially polarized focused light at $\lambda = 800$ nm. In the presence of metallic layer, the distance is taken as 5 nm above the metal layer. (b) A comparison of the frequency response of a prolate spheroid nanoparticle in the absence and presence of the metallic layer.

Acknowledgments

This work was performed with the support of the European Community Marie Curie International Reintegration Grant (IRG) Agreement Number MIRG-CT-2007-203690.